nature photonics
SUPPLEMENTARY INFORMATION
DOI: 10.1038/NPHOTON.2013.13

# Detecting Single Infrared Photons with 93 % System Efficiency: Supplementary Information

F. Marsili[1*], V. B. Verma[1], J. A. Stern[2], S. Harrington[1], A. E. Lita[1], T. Gerrits[1], I. Vayshenker[1], B. Baek[1], M. D. Shaw[2], R. P. Mirin[1], and S. W. Nam[1]

[1]National Institute of Standards and Technology, 325 Broadway, MC 815.04, Boulder, CO 80305, USA

[2]Jet Propulsion Laboratory, 4800 Oak Grove Dr., Pasadena, California 91109, USA

[*]corresponding author: francesco.marsili@nist.gov

## Table of contents

## List of characterized devices

Table SI 1 reports the details of the 28 devices we characterized so far. Table SI 1 reports, from left to right: fabrication run; nanowire width ($w$) and pitch ($p$); active area ($A_\mathrm{d}$); number of devices of the same type from the same fabrication run that were tested; number of devices of the same type from the same fabrication run that yielded; average and standard deviation of the switching current ($I_\mathrm{SW}$) of the yielded devices; average and standard deviation of the cut-off current ($I_\mathrm{co}$) of the yielded devices; average and standard deviation of the system detection efficiency ($SDE$) measured with the yielded devices.

**Table SI 1.** Details of the devices tested so far. The active area of the devices was either square or circular with diameter *D*. The values of *SDE* colored in blue have a relative uncertainty of 0.44 %. The values of *SDE* colored in red have a relative uncertainty of 4 %.

| Fabrication run | $w$ - $p$ (nm) | $A_d$ | Tested | Yielded | $I_{SW}$ (μA) | $I_{co}$ (μA) | *SDE* (%) |
|---|---|---|---|---|---|---|---|
| 1 | 110 - 220 | 15 μm × 15 μm | 2 | 2 | 6.6 ± 0.3 | 4.7 ± 0.4 | 86 ± 1 |
| 2 | 120 - 200 | 15 μm × 15 μm | 2 | 1 | 4 | 1.5 | 93 |
| 2 | 150 - 200 | $D$ = 15 μm | 1 | 1 | 6 | 3.2 | 90 |
| 3 | 130 - 200 | $D$ = 11 μm | 1 | 1 | 8.9 | 5.8 | 52 |
| 3 | 130 - 200 | $D$ = 13 μm | 1 | 1 | 8.4 | 5.2 | 75 |
| 3 | 130 - 180 | $D$ = 15 μm | 2 | 2 | 5.9 ± 0.3 | 3.8 ± 0.3 | 90 |
| 3 | 130 - 200 | $D$ = 15 μm | 1 | 1 | 8.5 | 5.3 | 79 |
| 4 | 130 - 180 | $D$ = 15 μm | 2 | 2 | 5.7 ± 0.1 | 3.4 ± 0.3 | 89.5 ± 0.7 |
| 4 | 150 - 200 | $D$ = 15 μm | 3 | 1 | 6 | 3.1 | 77 |
| 4 | 130 - 200 | $D$ = 15 μm | 1 | 0 | | | |
| 4 | 130 - 200 | $D$ = 11 μm | 1 | 0 | | | |
| 5 | 135 - 400 | $D$ = 18 μm | 4 | 4 | 7.7 ± 0.7 | 3.5 ± 0.8 | 87 ± 1 |
| 5 | 115 - 250 | $D$ = 20 μm | 1 | 1 | 6.7 | 2.8 | 90 |
| 5 | 115-250 | $D$ = 18 μm | 1 | 0 | | | |
| 5 | 140-250 | $D$ = 18 μm | 5 | 1 | 4.5 | 1.4 | 89 |

## Fabrication

Our WSi SNSPDs were fabricated on 200-nm-thick $SiO_2$ that was thermally grown on a 3 inch Si wafer. The WSi SNSPDs were embedded in an optical stack to enhance the absorption of the nanowires. The optical stack was composed by the following layers from top (illumination side) to bottom: $TiO_2$, $SiO_2$, WSi nanowires, $SiO_2$, and Au. After the deposition of the Au layer by thermal evaporation and of the $SiO_2$ layer by sputtering, the WSi film was deposited by co-sputtering W and Si targets[1], or by sputtering a

$W_{0.55}Si_{0.45}$ target, onto the substrate at room temperature. The stoichiometry of the films was estimated from the sputtering rates of W and Si for the co-sputtering deposition process and from the stoichiometry of the target for the sputtering deposition process. The WSi films had a resistivity of 200 ±20 μΩ·cm at 300 K. The thickness of the WSi film was 4 nm - 5 nm. The film had an amorphous structure as verified by x-ray diffraction[1] and high-resolution transmission electron microscopy (TEM). After depositing the film, the Ti / Au electrical contacts of each device were patterned by optical lithography to form a 50 Ω-matched coplanar transmission line. The nanowires were then patterned in a meander configuration by electron-beam lithography on a positive-tone (Poly(methyl methacrylate), PMMA) electron-beam resist and by etching in a $SF_6$ plasma. After fabricating the meander, the $SiO_2$ and $TiO_2$ layers were deposited by sputtering. A keyhole-shaped via was then etched through the substrate around the device as described in Ref. [2]. The nanowires were 100 nm to 200 nm wide, and the fill factor (the ratio between the width and the pitch of the nanowires) was varied from 50 % to 65 %. The active area of the device was either a 15 μm × 15 μm square or a 15 μm-diameter circle, allowing for efficient optical coupling of the device to a standard telecommunication single-mode fiber with a mode field diameter of 10 μm at 1550 nm.

## Measurement set-up

Figure SI 1 shows the schematics of the experimental set-up used for the optical characterization of our detector system (see Methods).

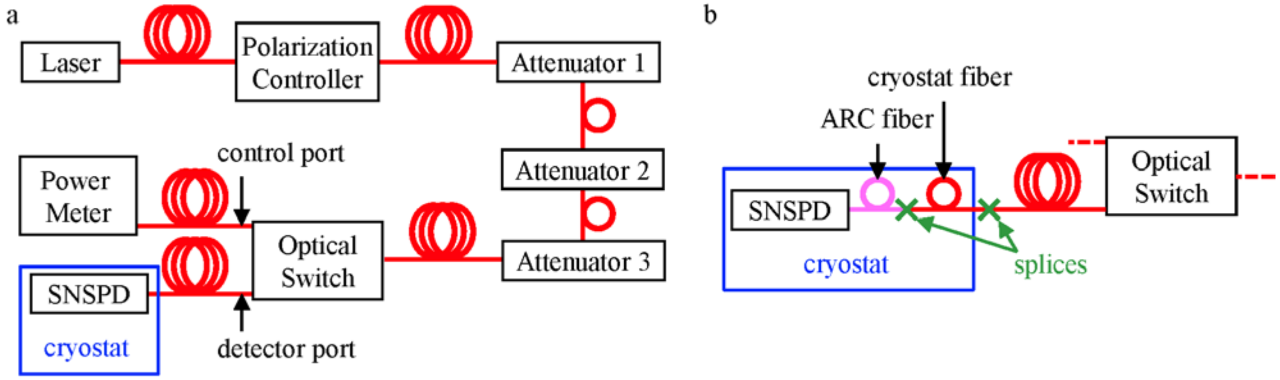

**Figure SI 1. a.** Schematics of the optical measurement set-up. The red lines represent silica C-band single-mode optical fibers. **b.** Detail of the optical coupling to the detector.

## Calibration of the optical power meters

The two optical power meters used to estimate the system detection efficiency (*SDE*) were calibrated by the Sources and Detectors Group group at NIST. The optical power meters were compensated for the spectral responsivity as described in Ref. [3] and for the nonlinearity as described in Ref. [4].

The power incident on an optical power meter ($P$) at a certain wavelength ($\lambda$) could be estimated from the display reading of the optical power meter ($P_{\mathrm{PM}}$) by using the absolute calibration factor ($CF_\lambda$) and the nonlinearity calibration factor ($CF_{\mathrm{NL}}$) at that wavelength: $P = P_{\mathrm{PM}} / CF_\lambda / CF_{\mathrm{NL}}$.

Figure SI 2a shows the wavelength dependence of $CF_\lambda$ (measured as reported in Ref. [3]) for the optical power meter at the control port of the optical switch (which we call *control power meter*; see Figure SI 1a) in the wavelength range $\lambda = 1510$ nm – 1630 nm. The other optical power meter, which we connected to the detector port of the optical switch to measure the splitting ratio (we call this optical power meter *detector power meter*, see section: Estimation of the system detection efficiency), was calibrated with the method described in Ref. [3] at $\lambda = 1549.6$ nm, as shown in Figure SI 2b (blue square). We determined the wavelength dependence of the absolute calibration of the detector power meter ($CF_{\lambda\mathrm{D}}$, red curve in Figure SI 2b) in the range $\lambda = 1510 – 1630$ nm by using the control power meter as a standard.

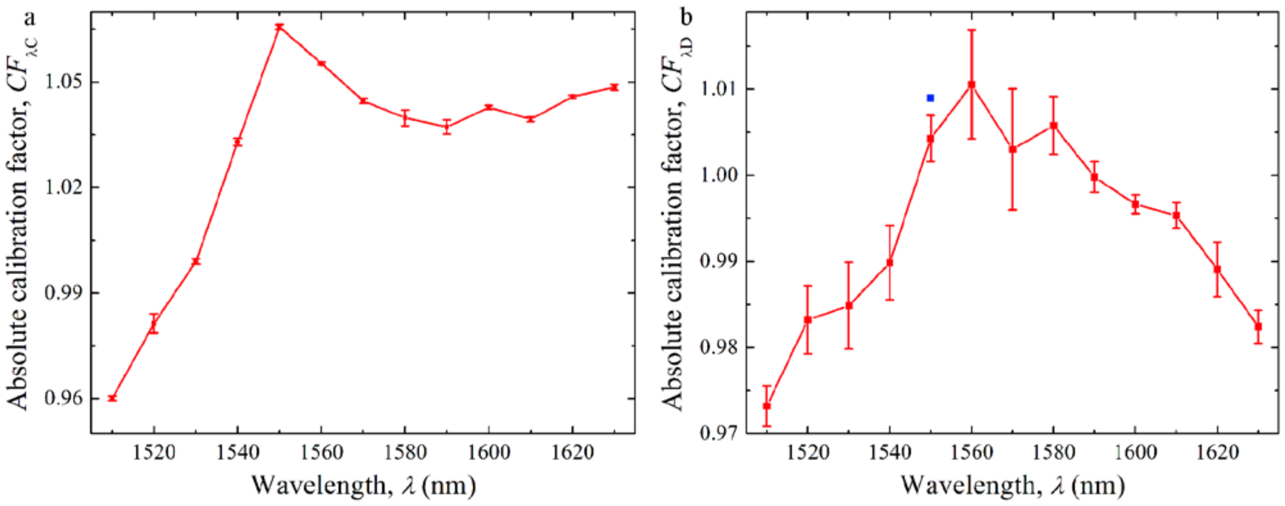

**Figure SI 2. a.** Wavelength dependence of $CF_{\lambda C}$ (determined as described in Ref. [3]) in the wavelength range $\lambda = 1510$ - $1630$ nm. $CF_{\lambda C}$ was determined at only one power level: $P = 100$ µW. The average value and the standard deviation of the $CF_{\lambda C}$ vs $\lambda$ curve were calculated on three subsequent acquisitions of the curve. **b.** Red curve: wavelength dependence of $CF_{\lambda D}$ (determined by using the control power meter as a standard) in the wavelength range $\lambda = 1510 – 1630$ nm. The average value and the standard deviation of the $CF_{\lambda D}$ vs $\lambda$ curve were obtained by averaging three subsequent acquisitions of the curve. Blue square: $CF_{\lambda D}$ (determined as described in Ref. [3]) for the detector power meter at $\lambda = 1549.6$ nm.

The nonlinearity calibration factor ($CF_{NL}(\lambda, r, P_{PM})$, where $r$ is the range of the optical power meter) was measured in the power range $P_{PM} = 1.5$ nW – 1.9 mW, spanning the six power ranges of our optical power meters ($r = 0, -10, -20, -30, -40, -50$ dBm). $CF_{NL}$ was measured at $\lambda = 1542$ nm for the control power meter and at $\lambda = 1550$ nm for the detector power meter. Figure SI 3 shows the power dependence of $CF_{NL}$ of the control power meter ($CF_{NLC}$, Figure SI 3a) and of the detector power meter ($CF_{NLD}$, Figure SI 3b) for the six power ranges available. Instead of compensating for the nonlinearity of the optical power meter by using the value of $CF_{NL}$ measured at a certain power and range, we used only one (power-independent) average correction factor for each range ($\langle CF_{NL}(r)\rangle$). The insets of Figure SI 3a and Figure SI 3b show the average and standard deviation of the nonlinearity correction factor at each power range calculated from the $CF_{NL}$ vs $P_{PM}$ curves. For both optical power meters, the $\langle CF_{NL}(r)\rangle$ varied by less than 1 % as a function of the power range.

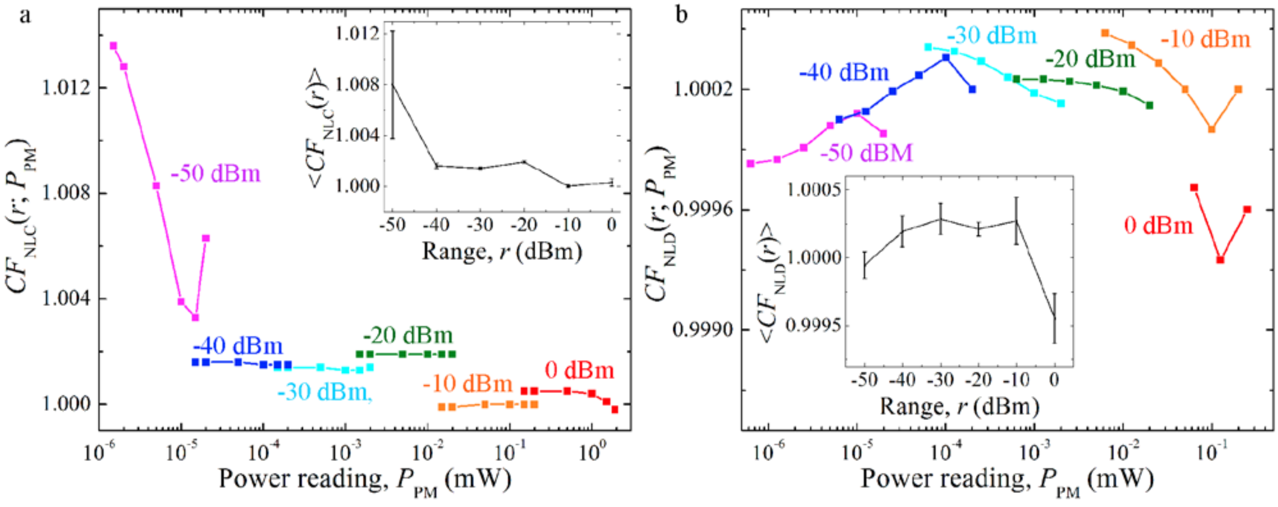

DOI: 10.1038/NPHOTON.2013.13

**Figure SI 3.** Nonlinearity correction factor ($CF_{\mathrm{NL}}$) vs power reading ($P_{\mathrm{PM}}$) at different power ranges ($r$ = 0, -10, -20, -30, -40, -50 dBm) for (a) the control power meter ($CF_{\mathrm{NLC}}$) and (b) the detector power meter ($CF_{\mathrm{NLD}}$). **Insets:** average and standard deviation of the nonlinearity correction factor at each power range for (a) the control power meter and (b) the detector power meter.

## Estimation of the system detection efficiency

The measurement of the system detection efficiency relies on the calibration of a variety of optical components (see Methods): optical power meters (see previous section), optical switch, and optical attenuators. In this section we describe the calibration of the optical switch and the optical attenuators.

Figure SI 4a shows the set-up used to measure the splitting ratio of the optical switch ($R_{\mathrm{SW}}$). We spliced the fiber of the detector port to a fiber terminated with a connector with the same anti-reflection coating (ARC) as the fiber coupled the SNSPD, and we coupled each of the ports of the optical switch to a calibrated optical power meter (see section: Calibration of the optical power meters). After setting the nominal attenuation of the three attenuators to 0 dB ($A_1 = A_2 = A_3 = 0$ dB), we measured the power at each of the ports of the optical switch as a function of wavelength in the range $\lambda = 1510\,\mathrm{nm} - 1630\,\mathrm{nm}$ and calculated the splitting ratio as: $R_{\mathrm{SW}}(\lambda) = P_{\mathrm{D}}(\lambda) / P_{\mathrm{C}}(\lambda)$, where $P_{\mathrm{D}}(\lambda)$ and $P_{\mathrm{C}}(\lambda)$ are the power measured by the detector and control power meters at wavelength $\lambda$. Figure SI 4b shows the wavelength dependence of $R_{\mathrm{SW}}$. After measuring $R_{\mathrm{SW}}$, we spliced the fiber of the detector port of the optical switch to the cryostat fiber.

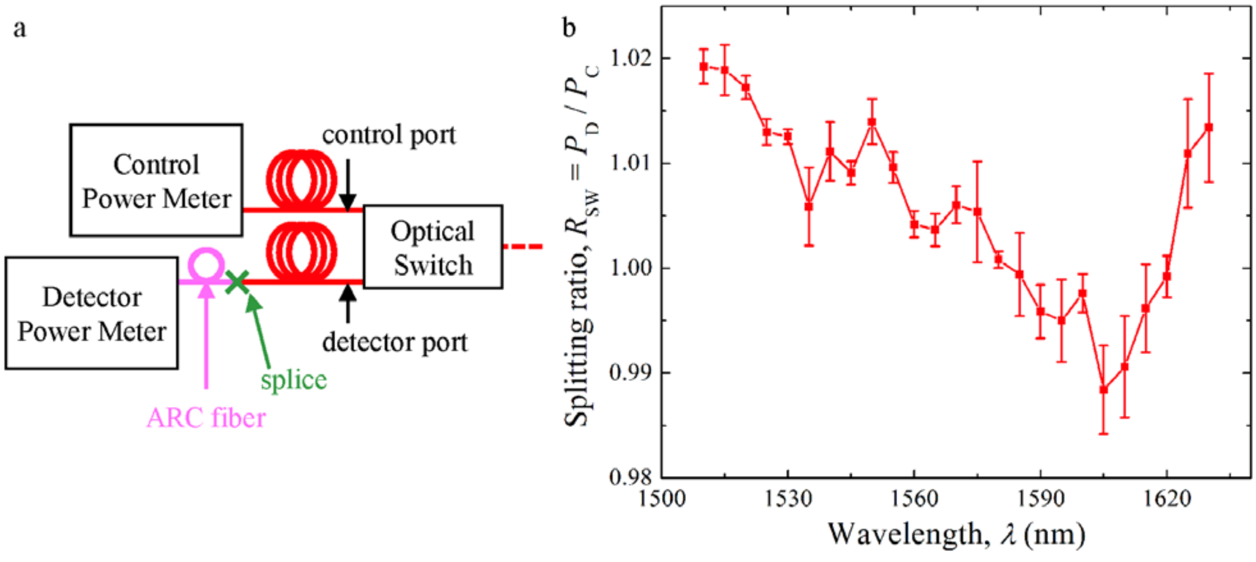

**Figure SI 4. a.** Detail of the set-up used to measure the wavelength dependence of the splitting ratio ($R_{\mathrm{SW}}$) of the optical switch. **b.** Wavelength dependence of the splitting ratio ($R_{\mathrm{SW}}$) of the optical switch. The average and standard deviation of the $R_{\mathrm{SW}}$ vs $\lambda$ curve were calculated on three subsequent acquisitions.

We measured the real attenuation at a certain wavelength of attenuator 2 ($\alpha_2$) and 3 ($\alpha_3$) when the nominal attenuation of attenuator 2 and 3 was set to 40 dB with the following procedure: (1) with the nominal attenuation of all the attenuators set to zero ($A_1 = A_2 = A_3 = 0$ dB), we diverted the light to the control port of the optical switch and measured the power ($P_{\mathrm{C0}}$); (2) we set the nominal attenuation of attenuator 2 to $A_2 = 40$ dB and measured the power at the control port of the optical switch ($P_{\mathrm{C2}}$); (3) we set the nominal attenuation of attenuator 2 to $A_2 = 0$ dB and the nominal attenuation of attenuator 3 to $A_3 = 40$ dB and measured the power at the control port of the optical switch ($P_{\mathrm{C3}}$); and (4) we estimated the real attenuation of the attenuators as $\alpha_2 = P_{\mathrm{C0}} / P_{\mathrm{C2}}$ and $\alpha_3 = P_{\mathrm{C0}} / P_{\mathrm{C3}}$. The method we adopted is only one of the possible ways to determine the real attenuation of our attenuators[5], which is heavily dependent upon careful calibration of the linearity of our optical power meter[1].

## Estimation of the uncertainty on the system detection efficiency

To estimate the uncertainty of the value of the *SDE* ($\sigma_{\mathrm{SDE}}$), we propagated the uncertainties on the measurements we performed to calculate the value of the *SDE*. We expressed the *SDE* as (see Methods): $SDE = PCR / [P_{\mathrm{C}} \cdot \alpha_2 \cdot \alpha_3 \cdot R_{\mathrm{SW}} / (1 - \rho) / E_{\lambda}]$, where $\rho$ is the reflectivity of the ARC fiber, and $E_{\lambda}$ is the energy of a single photon at wavelength $\lambda$. Assuming that all of the sources of uncertainty were independent, the relative uncertainty of *SDE* ($\sigma_{\mathrm{SDE}} / SDE$) is expressed as:

$$\left(\frac{\sigma_{\mathrm{SDE}}}{SDE}\right) = \sqrt{\left(\frac{\sigma_{\mathrm{PCR}}}{PCR}\right)^2 + \left(\frac{\sigma_{\mathrm{P_C}}}{P_{\mathrm{C}}}\right)^2 + 2\cdot\left(\frac{\sigma_{\alpha_{2,3}}}{\alpha_{2,3}}\right)^2 + \left(\frac{\sigma_{\mathrm{R_{SW}}}}{R_{\mathrm{SW}}}\right)^2}\ , \qquad (1)$$

where $\sigma_{\mathrm{PCR}}$ is the uncertainty of the photoresponse count rate (*PCR*); $\sigma_{\mathrm{P_C}}$ is the uncertainty of the power incident on the control power meter ($P_{\mathrm{C}}$); $\sigma_{\alpha_{2,3}}$ is the uncertainty of the attenuation of attenuator 2, 3 ($\alpha_{2,3}$); and $\sigma_{\mathrm{R_{SW}}}$ is the uncertainty of the splitting ratio of the optical switch ($R_{\mathrm{SW}}$). In equation (1) we neglected the uncertainty on $\rho$ and on $E_{\lambda}$, and we assumed the uncertainty on the attenuation of attenuators 2 and 3 to be identical.

DOI: 10.1038/NPHOTON.2013.13

We estimated the uncertainty on the value of the *SDE* only at $\lambda = 1550$ nm because: (1) the nonlinearity calibration factors of the control and detector power meters were measured only at $\lambda = 1542$ nm (for the control power meter) and $\lambda = 1550$ nm (for the detector power meter); and (2) the absolute calibration factor of the detector power meter was measured with the method described in Ref. [3] only at $\lambda = 1549.6$ nm. We assumed that the nonlinearity calibration factors at $\lambda = 1542$ nm did not differ significantly from the nonlinearity calibration factors at $\lambda = 1550$ nm and that the absolute calibration factor at $\lambda = 1549.6$ nm did not differ significantly from the absolute calibration factor at $\lambda = 1550$ nm.

### i. *Uncertainty of the photoresponse count rate*

The photoresponse count rate was calculated as $PCR = CR - SDCR$, where *CR* and *SDCR* are the average values calculated on six consecutive measurements. Therefore, the uncertainty of *PCR* ($\sigma_{\mathrm{PCR}}$) could be expressed as: $\sigma_{\mathrm{PCR}} = \sqrt{\sigma_{\mathrm{CR}}{}^2 + \sigma_{\mathrm{SDCR}}{}^2}$, where $\sigma_{\mathrm{CR}}$ is the uncertainty of the response pulse count rate (*CR*) and $\sigma_{\mathrm{SDCR}}$ is the uncertainty of the system dark-count rate (*SDCR*). The characterization of the stability of the optical components (see section: Stability of the optical components) indicates that the uncertainty on *CR* and *SDRC* was shot-noise-limited over the time scale of our measurements. Therefore, we estimated $\sigma_{\mathrm{CR}}$ and $\sigma_{\mathrm{SDCR}}$ by calculating the standard error of the mean on six consecutive measurements of the *CR* vs $I_{\mathrm{B}}$ and *SDCR* vs $I_{\mathrm{B}}$ curves. For $I_{\mathrm{B}} = 3$ µA, $\sigma_{\mathrm{PCR}} / PCR = 0.14$ %.

### ii. *Uncertainty of the power incident on the control power meter*

The power incident on the control power meter ($P_{\mathrm{C}}$) was estimated from one single display reading of the optical power meter ($P_{\mathrm{PMC}}$) as: $P_{\mathrm{C}} = P_{\mathrm{PMC}} / CF_{\lambda\mathrm{C}} / \langle CF_{\mathrm{NLC}}(r)\rangle$ (see Methods and section: Estimation of the system detection efficiency). The optical power used was typically $P_{\mathrm{PMC}} \approx 0.5$ µW, and the optical power meter range was $r = -30$ dBm. Therefore, the relative uncertainty of $P_{\mathrm{C}}$ ($\sigma_{\mathrm{P_C}} / P_{\mathrm{C}}$) could be expressed as:

$$\left(\frac{\sigma_{\mathrm{P_C}}}{P_{\mathrm{C}}}\right) = \sqrt{\left(\frac{\sigma_{\mathrm{P_{PMC}}}}{P_{\mathrm{PMC}}}\right)^2 + \left(\frac{\sigma_{\mathrm{CF_{\lambda C}}}}{CF_{\lambda\mathrm{C}}}\right)^2 + \left(\frac{\sigma_{\mathrm{CF_{NLC}}}}{<CF_{\mathrm{NLC}}(-30\ \mathrm{dBm})>}\right)^2}\ .$$

The relative uncertainty of $P_{\mathrm{PMC}}$ was estimated by calculating the standard deviation on six consecutive measurements of $P_{\mathrm{PMC}}$: $\sigma_{\mathrm{P_{CPM}}} / P_{\mathrm{CPM}} = 0.15$ %. The relative uncertainty of $CF_{\lambda\mathrm{C}}$ was obtained by propagating the uncertainty due to the repeatability of the measurement of $CF_{\lambda C}$ (standard error of the mean of 0.03 %, see Figure SI 2a) and the uncertainty inherent to the calibration method [3] (0.13 %): $\sigma_{\mathrm{CF}_{\lambda C}} / CF_{\lambda C} = 0.14\ \%$. The relative uncertainty of $CF_{\mathrm{NLC}}$ was obtained by propagating the standard error of the mean of <$CF_{\mathrm{NLC}}$(-30 dBm)> (0.004 %, see Figure SI 3a) and the uncertainty inherent to the calibration method[4] (0.02 %): $\sigma_{\mathrm{CF}_{\mathrm{NLC}}} / < CF_{\mathrm{NLC}}(-30\ \mathrm{dBm}) >= 0.02\ \%$.

### iii. *Uncertainty of the attenuation*

The real attenuation of attenuator 2 ($\alpha_2$) and attenuator 3 ($\alpha_3$) were estimated from the display reading of the control power meter ($P_{\mathrm{PMC}}$) as (see Methods and section: Estimation of the system detection efficiency):

$$\alpha_i = \alpha_{\mathrm{PM}i} \cdot \frac{<CF_{\mathrm{NLC}}(r_i)>}{<CF_{\mathrm{NLC}}(r_0)>} \qquad \text{for } i = 2, 3 \qquad ,$$

where $\alpha_{\mathrm{PM}i} = P_{\mathrm{PMC0}} / P_{\mathrm{PMC}i}$; $P_{\mathrm{PMC0}} \approx 70\ \mu\mathrm{W}$ was the display reading of the control power meter with the nominal attenuation of all the attenuators set to zero ($A_1 = A_2 = A_3 = 0$ dB); $P_{\mathrm{PMC}i} \approx 7$ nW was the display reading of the control power meter with the nominal attenuation of attenuator $i$ set to $A_i = 40$ dB; $r_0 = -10$ dBm; and $r_i = -50$ dBm. Therefore, the relative uncertainty of $\alpha_i$ ($\sigma_{\alpha_i} / \alpha_i$) could be expressed as:

$$\left(\frac{\sigma_{\alpha_i}}{\alpha_i}\right) = \sqrt{\left(\frac{\sigma_{\alpha_{\mathrm{PM}i}}}{\alpha_{\mathrm{PM}i}}\right)^2 + \left(\frac{\sigma_{\mathrm{CF}_{\mathrm{NLC}}}}{<CF_{\mathrm{NLC}}(-10\ \mathrm{dBm})>}\right)^2 + \left(\frac{\sigma_{\mathrm{CF}_{\mathrm{NLC}}}}{<CF_{\mathrm{NLC}}(-50\ \mathrm{dBm})>}\right)^2} \qquad .$$

The relative uncertainty of $\alpha_{\mathrm{PMi}}$ was due to the repeatability of the measurement and was estimated by calculating the standard deviation on six consecutive measurements of $\alpha_{\mathrm{i}}$: $\sigma_{\alpha_{\mathrm{PMi}}} / \alpha_{\mathrm{PMi}} = 0.15\ \%$. The relative uncertainty of $CF_{\mathrm{NLC}}$ at the two ranges was obtained by propagating the standard error of the mean of <$CF_{\mathrm{NLC}}$(-10 dBm)> (0.004 %, see Figure SI 3a) or <$CF_{\mathrm{NLC}}$(-50 dBm)> (0.17 %, see Figure SI 3a) and the uncertainty inherent to the calibration method: $\sigma_{\mathrm{CF}_{\mathrm{NLC}}} / < CF_{\mathrm{NLC}}(-10\ \mathrm{dBm}) >= 0.02\ \%$ and $\sigma_{\mathrm{CF}_{\mathrm{NLC}}} / < CF_{\mathrm{NLC}}(-50\ \mathrm{dBm}) >= 0.17\ \%$.

### iv. *Uncertainty of the splitting ratio*

The splitting ratio of the optical switch ($R_{\mathrm{SW}}$) was estimated by averaging three consecutive display readings of the control ($P_{\mathrm{PMC}} \approx 70\ \mu\mathrm{W}$) and detector ($P_{\mathrm{PMD}} \approx 70\ \mu\mathrm{W}$) power meters as (see Methods and section: Estimation of the system detection efficiency):

DOI: 10.1038/NPHOTON.2013.13

$$R_{\mathrm{SW}} = R_{\mathrm{SWPM}} \cdot \frac{<CF_{\mathrm{NLC}}(r)>}{<CF_{\mathrm{NLD}}(r)>} \cdot \frac{CF_{\lambda\mathrm{C}}}{CF_{\lambda\mathrm{D}}} \qquad ,$$

where $R_{\mathrm{SWPM}} = P_{\mathrm{PMD}} / P_{\mathrm{PMC}}$ and $r = -10$ dBm. Therefore, the relative uncertainty of $R_{\mathrm{SW}}$ ($\sigma_{\mathrm{R_{SW}}} / R_{\mathrm{SW}}$) could be expressed as:

$$\left(\frac{\sigma_{\mathrm{R_{SW}}}}{R_{\mathrm{SW}}}\right) = \sqrt{\left(\frac{\sigma_{\mathrm{R_{SWPM}}}}{R_{\mathrm{SWPM}}}\right)^2 + \left(\frac{\sigma_{\mathrm{CF_{NLC}}}}{<CF_{\mathrm{NLC}}(-10\ \mathrm{dBm})>}\right)^2 + \left(\frac{\sigma_{\mathrm{CF_{NLD}}}}{<CF_{\mathrm{NLD}}(-10\ \mathrm{dBm})>}\right)^2 + \left(\frac{\sigma_{\mathrm{CF_{\lambda C}}}}{CF_{\lambda\mathrm{C}}}\right)^2 + \left(\frac{\sigma_{\mathrm{CF_{\lambda D}}}}{CF_{\lambda\mathrm{D}}}\right)^2} \quad .$$

The relative uncertainty of $R_{\mathrm{SWPM}}$ was due to the repeatability of the measurement and was estimated by calculating the standard error of the mean on three consecutive measurements of $R_{\mathrm{SW}}$ (see Figure SI 4b): $\sigma_{\mathrm{R_{SWPM}}} / R_{\mathrm{SWPM}} = 0.08\ \%$. The relative uncertainty deviation of $CF_{\mathrm{NL}}$ and $CF_{\lambda}$ for the two optical power meters were obtained as described above.

**Table SI 2** summarizes the relative uncertainty of each of the measurements performed to obtain the *SDE*. By using equation (1), we obtained $\sigma_{\mathrm{SDE}} / SDE = 0.44\ \%$.

**Table SI 2.** Relative uncertainty of the measurements performed to obtain the *SDE*.

| source | relative uncertainty (%) |
|---|---|
| *PCR* | 0.14 |
| $P_{\mathrm{C}}$ | 0.20 |
| $\alpha_{\mathrm{i}}$ | 0.20 |
| $R_{\mathrm{SW}}$ | 0.22 |

## Stability of the optical components

While measuring the *SDE*, the stability of the optical components can affect the uncertainty of the measurement. Therefore, we continuously measured the optical power of the laser ($P$), the real attenuation of the attenuators ($\alpha$), and the splitting ratio of the MEMS optical switch ($R_{\mathrm{SW}}$) at $\lambda = 1550$ nm over an extended period to verify that they were stable for the duration of the *SDE* measurement. We used the Allan variance[6] to characterize the stability of our system:

$$\sigma_{\mathrm{y}}^{2}(t_{\mathrm{a}}) = \frac{1}{N}\sum_{i=1}^{N-1}\frac{[\bar{y}_{i+1}-\bar{y}_{i}]^{2}}{2} \quad , \qquad (1)$$

where $\bar{y}_i$ is the $i$th measurement (sampling) of quantity $y$ averaged over an averaging time $t_{\mathrm{a}}$ and $N$ is the total number of measurements. The averaging time at which the Allan variance is minimum corresponds to the optimum averaging time that can be adopted to reduce the uncertainty of the measurement of $y$.

We measured the power of the laser ($P$) over extended periods (longer than 10 hours) by using different integration times of the optical power meter ($t_{\mathrm{PM}}$, the period over which the optical power meter averages the power before displaying a power reading). The data were sampled after each integration time $t_{\mathrm{PM}}$ and transferred to the computer. The optical power meter was not compensated for the drift of the dark current during each of the measurements. Figure SI 5a shows the $P$ vs time curve measured over a ≈ 15-hour period with $t_{\mathrm{PM}} = 1$ s. As shown in Figure SI 5b, the histogram of the values of the measured power did not fit a Gaussian curve, as we would expect if the measurement of the power was affected only by Gaussian noise. Figure SI 5c shows the Allan variance of the laser power ($\sigma_{\mathrm{P}}^{2}$) as a function of the averaging time ($t_{\mathrm{a}}$) measured with different integration times of the optical power meter ($t_{\mathrm{PM}}$). We calculated the value of $\sigma_{\mathrm{P}}^{2}$ for a certain $t_{\mathrm{a}}$ and $t_{\mathrm{PM}}$ with the following procedure: (1) we re-binned the power readings acquired with integration time $t_{\mathrm{PM}}$ into adjacent time intervals of duration $t_{\mathrm{a}}$; (2) we calculated the average value of the power readings within each of the bins (thus obtaining $\overline{P}_i$ for the $i^{\mathrm{th}}$ bin); (3) we used equation (1) to calculate $\sigma_{\mathrm{P}}^{2}(t_{\mathrm{a}})$. For the short averaging times, the upward slope at low integration times was unexpected. The initial rise for short averaging times could be caused by the correlation of successive measurements due to sampling at a rate higher than the true averaging time[2] or by mode-hopping of the laser beam. The position of the minimum of the Allan variance curve indicates that the laser and power meter system was stable for ≈ 100 s, which was shorter than the period needed to perform the *SDE* measurements and the other measurements made to characterize the optical components in our setup (see section: Estimation of the system detection efficiency). For example, the power measurements used to estimate the *SDE* were performed with the following procedure: (1) the power meter was zeroed with the shutters of the three attenuators closed; (2) the shutters were opened and the laser power incident on the power meter was measured with $t_{\mathrm{PM}} = 2$ s. The variation as measured by the Allan variance and standard deviation is much less than 0.1 %.

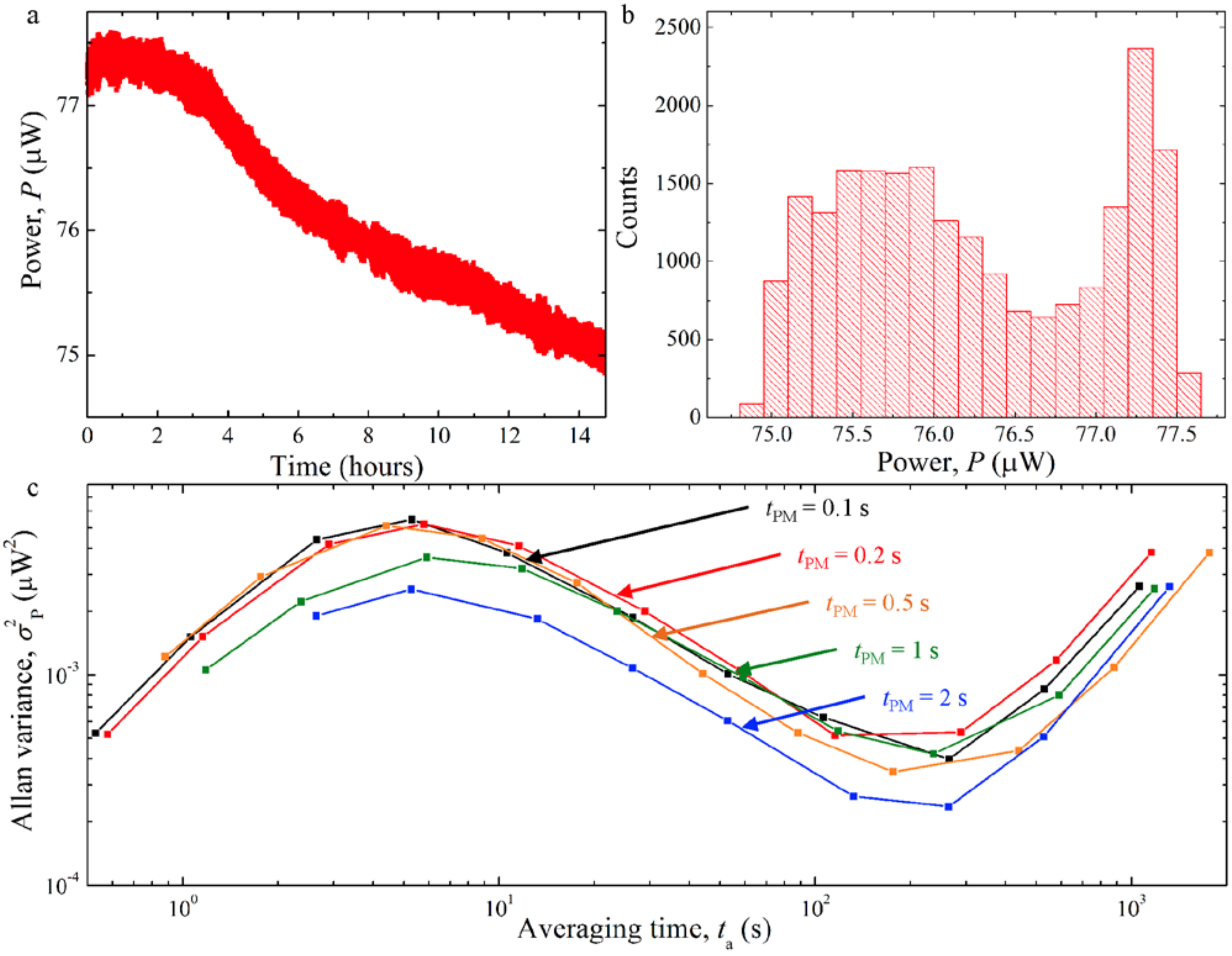

**Figure SI 5. a.** Laser power ($P$) measured for ≈ 15 hours with $t_{\mathrm{PM}} = 1$ s. **b.** Histogram of the laser power data shown in panel a. **c.** Allan variance of the power of the laser light ($\sigma_{\mathrm{P}}^2$) vs averaging time ($t_{\mathrm{a}}$) for different power meter integration times ($t_{\mathrm{PM}}$).

Measuring the *SDE* also required attenuators and a MEMS optical switch. Therefore, we characterized the stability of the real attenuation of the attenuators ($\alpha$), and of the splitting ratio of the optical switch ($R_{\mathrm{SW}}$) over an extended period to verify that they were stable for the duration of the *SDE* measurement. Figure SI 6a shows the measurement over a 16-hour period of the real attenuation of the attenuators ($\alpha$) when the nominal attenuation was set to $A_1 = 0$ dB and $A_2 = A_3 = 40$ dB. Figure SI 6b shows the histogram of $\alpha$ (red bars) and its Gaussian fit (black line). In Figure SI 6c, the stability of the splitting ratio of the optical switch can be observed over a 15 hour measurement period. Figure SI 6d shows the histogram of $R_{\mathrm{SW}}$ (red bars) and its Gaussian fit (black line). Both the histogram of α and of $R_{SW}$ display a Gaussian shape. Over our maximum measurement period, the standard deviations of α and $R_{SW}$ were 0.15 % and 0.17 % of the mean respectively.

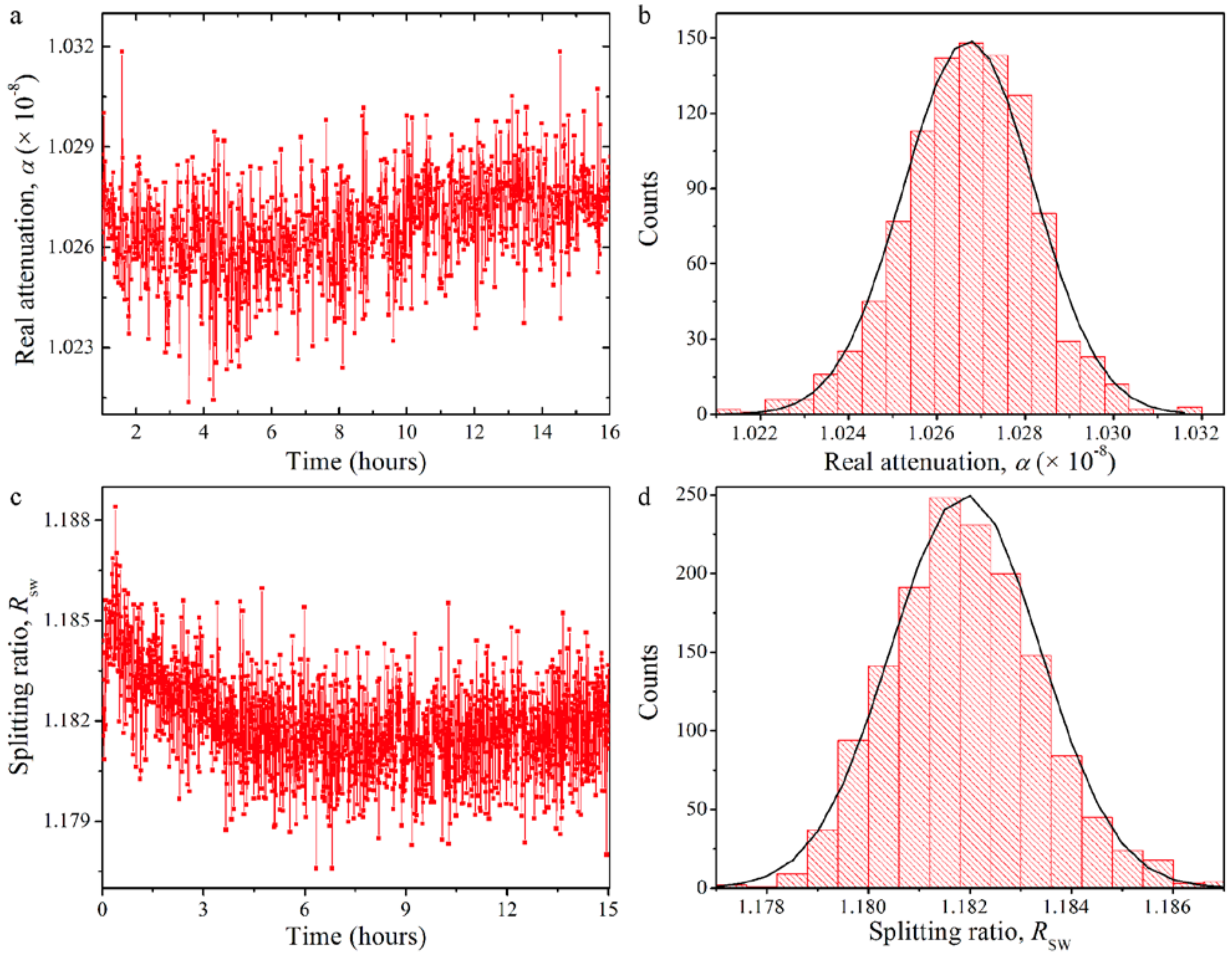

**Figure SI 6. a.** Real attenuation of the attenuators ($\alpha$), over 16 hours. **b.** Histogram of $\alpha$ (red bars) and its Gaussian fit (black line). **c.** Splitting ratio ($R_{SW}$) of the MEMS optical switch for a 15 hour measurement period. **d.** Histogram of $R_{SW}$ (red bars) and its Gaussian fit (black line).

## Optical simulations of the system detection efficiency

We fitted the experimental *SDE* curves shown in Figure 2c by using rigorous coupled-wave analysis (RCWA) calculations[7] of the wavelength and polarization dependence of the absorption of the optical stack. In our fitting, we used four free parameters: (1) the thickness of the $TiO_2$ layer on top of the optical

DOI: 10.1038/NPHOTON.2013.13

stack (see section: Fabrication); (2) the thickness and width of the WSi nanowires, and (3) the coupling losses. The fitting curves for $SDE_{\max}$, $SDE_{\min}$ and $R$ are shown in Figure SI 7. The fitting parameters differed from the measured parameter of the optical stack by less than 15 % (see caption of Figure SI 7).

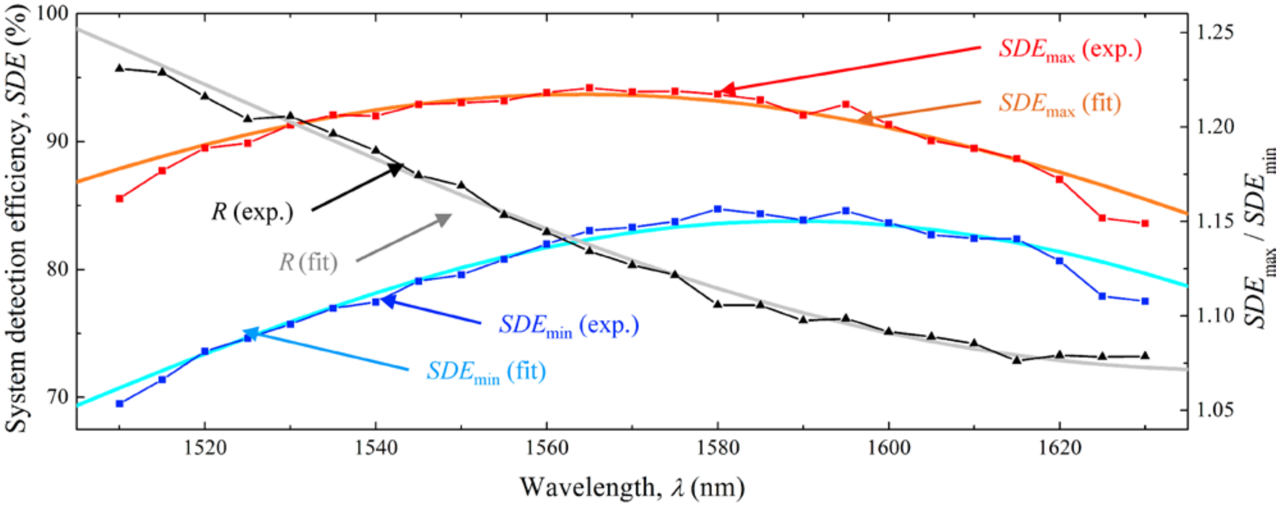

**Figure SI 7.** Experimental and fitted wavelength dependence of the maximum *SDE* ($SDE_{\max}$), of the minimum *SDE* ($SDE_{\min}$) and of the ratio $R = SDE_{\max} / SDE_{\min}$. The measured parameters of the optical stack were, from top (illumination side) to bottom: 213 nm-thick $TiO_2$; 231 nm-thick $SiO_2$; 4.5 nm-thick, 120 nm-wide WSi nanowires with 200 nm pitch; 230 nm-thick $SiO_2$; 80 nm-thick Au. The parameters that fitted the experimental data were: 226 nm-thick $TiO_2$; 4.3 nm-thick, 102 nm-wide WSi nanowires with 200 nm pitch; 3.8 % coupling losses.

## Refractive indexes of the materials employed in the optical stack

We measured the refractive index of $TiO_2$, $SiO_2$ and WSi films in the wavelength range $\lambda = 1$ - 2 μm with a variable-angle spectroscopic ellipsometer. The refractive index of WSi ($N_{\mathrm{WSi}}$) was measured on the following sample (from top, illumination side, to bottom): 5.5 nm-thick WSi deposited by cosputtering (see section: Fabrication); 240 nm-thick sputtered $SiO_2$; Si substrate. The refractive index of $SiO_2$ ($N_{\mathrm{SiO_2}}$) was measured on a 240 nm-thick $SiO_2$ layer sputtered on a Si substrate. The refractive index of $TiO_2$ ($N_{\mathrm{TiO_2}}$) was measured on a 75 nm-thick $TiO_2$ layer sputtered on a Si substrate. We used the data reported in Ref.[8] to model the wavelength dependence of the refractive index of Au. The device reported in the paper was fabricated with WSi deposited by sputtering of a stoichiometric target, whose refractive index was not characterized. Figure SI 8 shows the wavelength dependence of (a) $N_{\mathrm{WSi}}$, (b) $N_{\mathrm{SiO_2}}$, and (c) $N_{\mathrm{TiO_2}}$.

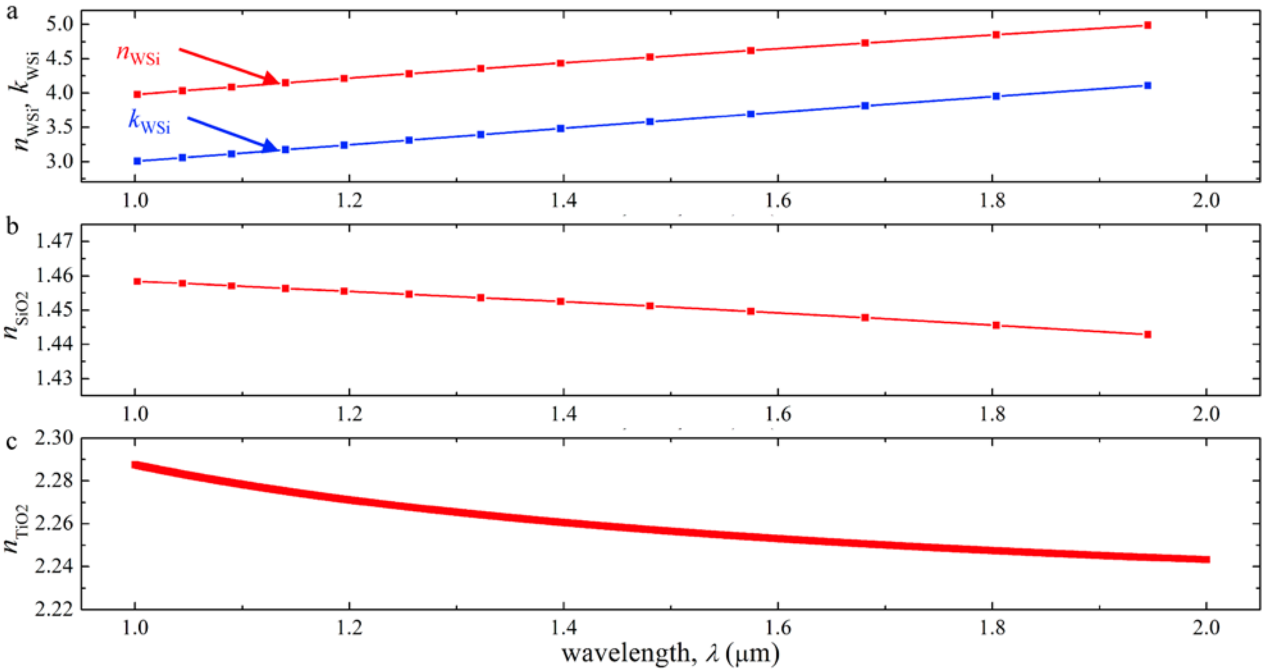

**Figure SI 8.** Wavelength dependence of the index of refraction (*n*) and of the extinction coefficient (*k*) of (a) WSi, (b) $SiO_2$, and (c) $TiO_2$.

## Noise contribution to the jitter

The jitter of our detector system (which we call *system jitter*, $J_S$) was due to two contributions, which added in quadrature: (1) the intrinsic jitter of the detector ($J_d$); and (2) the jitter due to the electrical noise of the read out, which we call *noise contribution to the jitter* ($J_n$). $J_S$ is then expressed as: $J_S = \left(J_d^2 + J_n^2\right)^{1/2}$.

The noise contribution to the jitter was larger for our detector system than for conventional NbN SNSPDs[9] because of the longer rise time (by a factor of ≈ 10 with respect to 10 µm × 10 µm-active-area NbN SNSPDs) and lower switching current (by a factor of ≈ 5) of our WSi SNSPDs. We estimated the noise contribution to the jitter as: $J_n = e_n / S$ (see e.g. Ref. [10]), where $e_n$ is the FWHM of the electrical noise and $S$ is the slope of the rising edge of the response pulse of the SNSPD. Figure SI 9 shows the current dependence of the system jitter ($J_S$, blue curve) and of $J_n$ (red curve). The expression of $J_n$ provided an estimate of the order of magnitude of the noise-induced

DOI: 10.1038/NPHOTON.2013.13

jitter, so the fact that $(J_S^2 - J_n^2)^{1/2} < 100$ ps over the whole bias range investigated could be interpreted only as a qualitative indication that the electrical noise of the read out was the dominant component of $J_S$.

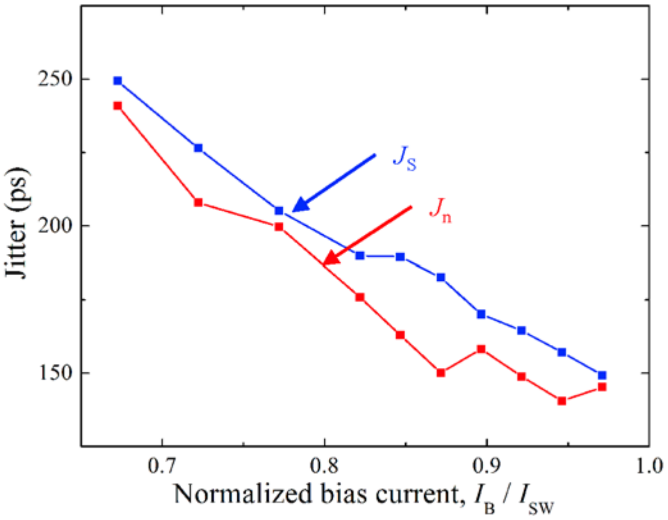

**Figure SI 9.** Bias-current dependence of the jitter of the detector system ($J_S$, blue curve) and of the noise contribution to the jitter ($J_n$).

To further support our claim, we measured the system detection efficiency (*SDE*) and the system jitter ($J_S$) using an SNSPD from a different fabrication batch and with higher switching current ($I_{SW}$ = 6.5 µA; we call this device *SNSPD$_2$*) than the device reported in the body of the paper ($I_{SW}$ = 4 µA; we call this device *SNSPD$_1$*). SNSPD$_2$ was based on 120 nm-wide, 5 nm-thick nanowires arranged in a meander pattern with 220 nm pitch. The active area of SNSPD$_2$ was a 15 µm × 15 µm square.

Figure SI 10a shows the bias dependence of the *SDE* (red curve) and of the *SDCR* (black curve) measured with SNSPD$_2$. The polarization state of the light was varied to maximize the *SDE*. The cut-off current ($I_{co}$) of the *SDE* vs $I_B$ curve measured with SNSPD$_2$ was $I_{co} = 0.74 I_{SW}$, higher by approximately a factor of 2 than the cut-off current measured with SNSPD$_1$ ($I_{co} = 0.37 I_{SW}$, see Figure 1a). The difference in $I_{co}$ between SNSPD$_2$ and SNSPD$_1$ indicates that although the superconducting cross-section of the nanowires of the two devices was expected to be similar (within 10 %, based on the deposition time of the WSi films and on the SEM image of the nanowires) the superconducting cross-section was larger in SNSPD$_2$ than in SNSPD$_1$, which could also explain the difference in $I_{SW}$ between the two devices. We attributed this discrepancy to the fact that our estimate of the superconducting cross section of the nanowires was inaccurate due to the following reasons: (1) the deposition rate in two different deposition runs can be different; (2) the thickness of the WSi across the 3 inch wafer may be subject to variations (from resistivity measurements, we estimated a thickness variation of 25 % within a 1.1 inch radius from the center of the wafer); (3) as 3 inch wafers are not perfectly flat, the focus of the electron beam may change across the wafer, which may cause the nanowire width to change across the wafer.

We characterized the timing performance of the detector system employing SNSPD$_2$ by using two different read-out schemes: the room-temperature electronics (see Methods) and a cryogenic preamplifier stage (5 – 800 MHz bandwidth). Figure SI 10b shows the instrument response function (IRF) measured with the room-temperature (blue curve) and cryogenic electronics (orange curve) at a bias current of $I_\mathrm{B} = I_\mathrm{SW}$. The system jitter decreased form $J_\mathrm{S} = 121$ ps with the room-temperature electronics to $J_\mathrm{S} = 96$ ps with the cryogenic preamplifier. We attributed the improvement of $J_\mathrm{S}$ to the decrease of the jitter due to the reduction in electrical noise, as indicated by the fact that $J_\mathrm{n}$ decreased form $J_\mathrm{n} = 94$ ps with the room-temperature electronics to $J_\mathrm{n} = 60$ ps with the cryogenic preamplifier.

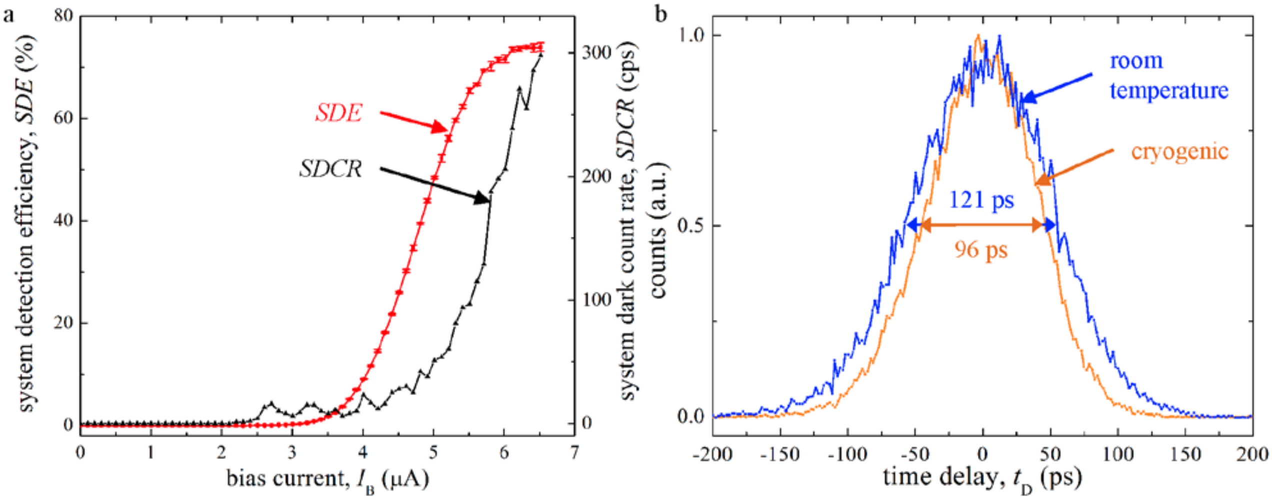

**Figure SI 10. a.** System detection efficiency (*SDE*, red curve) and system dark-count rate (*SDCR*, black curve) vs bias current ($I_\mathrm{B}$) at $\lambda = 1550$ nm and $T = 120$ mK for SNSPD$_2$. The average and the standard deviation of the *SDE* vs $I_\mathrm{B}$ curve were calculated on 4 subsequent acquisitions of the curve. **b.** Instrument response function (IRF) of SNSPD$_2$ biased at $I_\mathrm{B} = I_\mathrm{SW}$ measured with the room temperature (blue curve) and cryogenic (orange curve) read out. The time delay ($t_\mathrm{D}$) was measured between the synchronization pulse of the mode-locked laser and the SNSPD pulse. The IRF was normalized by its maximum. The horizontal arrows indicate the full width at half maximum (FWHM) of the two IRFs.

## References

1 Baek, B., Lita, A. E., Verma, V. & Nam, S. W. Superconducting a-$W_xSi_{1-x}$ nanowire single-photon detector with saturated internal quantum efficiency from visible to 1850 nm. *Appl. Phys. Lett.* **98**, 251105-251103 (2011).

2 Miller, A. J. *et al.* Compact cryogenic self-aligning fiber-to-detector coupling with losses below one percent. *Opt. Express* **19**, 9102-9110 (2011).

3 Vayshenker, I., Li, X., Livigni, D. J., Scott, T. R. & Cromer, C. L. Optical fiber power meter calibrations at NIST. *NIST Special Publication* **250-54** (2000).

4 Vayshenker, I., Yang, S., Li, X., Scott, T. R. & Cromer, C. L. Optical fiber power meter nonlinearity calibrations at NIST. 250-256 (2000).

5 Yang, S., Vayshenker, I., Li, X. & Scott, T. R. Optical detector nonlinearity: a comparison of five methods. *Digest, Conf. Precision Electromagnetic Measurements*, 455-456 (1994).

6 Allan, D. Statistics of Atomic Frequency Standards. *Proceedings of IEEE* **54**, 221-230 (1966).

7 Zinoni, C. *et al.* Single-photon experiments at telecommunication wavelengths using nanowire superconducting detectors. *Appl. Phys. Lett.* **91**, 031106-031103 (2007).

8 Palik , E. D. in *Handbook of Optical Constants of Solids* Vol. I 289 (Academic Press, 1998).

9 Natarajan, C. M., Tanner, M. G. & Hadfield, R. H. Superconducting nanowire single-photon detectors: physics and applications. *Supercond. Sci. Technol.* **25**, 063001 (2012).

10 ORTEC. Application note AN42. *http://www.ortec-online.com*.